Title	Deformation mechanisms of selective laser melted 316L austenitic stainless steel in high temperature low cycle fatigue
Author(s)	Chen, Yefeng; Wang, Xiaowei; Shen, Jiawei; Peng, Yawei; Jiang, Yong; Yang, Xinyu; Leen, Sean B.; Gong, Jianming
Publication Date	2022-04-22
Publication Information	Chen, Yefeng, Wang, Xiaowei, shen, Jiawei, Peng, Yawei, Jiang, Yong, Yang, Xinyu, Leen, Sean B., Gong, Jianming. (2022). Deformation mechanisms of selective laser melted 316L austenitic stainless steel in high temperature low cycle fatigue. Materials Science and Engineering: A, 843, 143123. doi:https://doi.org/10.1016/j.msea.2022.143123
Publisher	Elsevier
Link to publisher's version	https://doi.org/10.1016/j.msea.2022.143123
Item record	http://hdl.handle.net/10379/17348
DOI	http://dx.doi.org/10.1016/j.msea.2022.143123

Deformation mechanisms of selective laser melted 316L austenitic stainless steel in high temperature low cycle fatigue

Yefeng Chen[a,b], Xiaowei Wang[a,b,], Jiawei shen[a,b], Yawei Peng[a,b], Yong Jiang[a,b], Xinyu Yang[c], Sean B.Leen[c], Jianming Gong[a,b,*]*

[a] *School of Mechanical and Power Engineering, Nanjing Tech University, Nanjing 211816, PR China;*

[b] *Jiangsu Key Lab of Design and Manufacture of Extreme Pressure Equipment, Nanjing 211816, PR China;*

[c]*Mechanical Engineering, School of Engineering, College of Science and Engineering, NUI Galway, Ireland*

***Corresponding authors:**

E-mail: *xwwang@njtech.edu.cn (Xiaowei Wang); gongjm@njtech.edu.cn (Jianming Gong)*

Abstract

To investigate the low cycle fatigue (LCF) properties of SLM (Selective laser melting) 316L at 550℃ high temperature, a series of LCF tests at different strain amplitudes is conducted on SLM 316L and traditional 316L. In contrast to the cyclic hardening behavior of traditional 316L, SLM 316L is shown to have a stable cyclic softening behavior and higher fatigue life due to its higher strength (yield strength is 1.9 times of traditional 316L). The coarsening of cellular sub-structure, evolution of geometrically necessary dislocations (GND) and texture direction contribute to the cyclic softening behavior of SLM 316L. Fractographic observations illustrate that strain amplitude has a significant influence on initiation and propagation of transgranular fatigue cracks, and lack-of-fusion defects near the surface are key initiation sites of fatigue cracks. Additionally, the life prediction method of the non-Masing model is suitable for SLM 316L.

***Key words**:*

Low cycle fatigue; High temperature; Selective laser melting; Microstructure evolution; 316L stainless steel

1. Introduction

As a realistic alternative to many conventional manufacturing techniques, selective laser melting (SLM) has attracted much attention. Due to numerous advantages including rapid manufacturing, high accuracy and high complexity [1, 2]**,** SLM has been applied in many critical areas such as aerospace [3], biomedical engineering [4],

and nuclear power plants [5]. It is well known that SLM provides a good combination of mechanical properties and complex geometry, because of the near full-density of the layer-by-layer fabricating process [6]. Furthermore, compared with other metal additive manufacturing methods, SLM has higher accuracy and lower roughness resulting from smaller melting spot, thinner layers, and finer powder [7]. Therefore, SLM materials are currently the focus of significant research.

Among several austenitic stainless steels (ASS), 316L stainless steel, in particular, has a good combination of high-temperature tensile properties and creep strength, corrosion resistance, irradiation damage resistance. Thus, it has been adopted as a structural material in several high-temperature components such as the primary side of liquid metal cooled fast breeder reactor (LMFBR) [8]. In these applications, the components are usually exposed to high temperatures (300-600℃) and subjected to complex thermo-mechanical loading [9], especially for the instrument valves. Normally, instrument valves have complicated inner channels, which are costly and difficult to manufacture by conventional methods. Hence SLM, a near net-shaped manufacturing technology, is an ideal method to fabricate such components [10]. Considering the severe operating conditions, compounded by the requirement for safe operation over a 50 year life-span in nuclear plant, fatigue damage must be addressed in design and evaluation [11]. The low cycle fatigue (LCF) properties of conventional manufactured 316L stainless steel under high temperature have been widely studied in the past few decades [12-18]. In the temperature range 500-600℃, the 316L(N) has exhibit cyclic hardening behavior [19] resulted from the individual or combined effects of dislocation interactions with (a) other dislocations (b) precipitates and (c) solute atoms [15]. Srinivasan et al [20] reported that 316L(N) exhibits cyclic softening behavior at 600 ℃ after 20% strain cold work, due to its high density of dislocations. However, there are very few studies about LCF properties of SLM 316L. To facilitate increased uptake of SLM technology for these critical areas, there is an urgent need for systematic investigation of the high temperature LCF properties of SLM 316L.

Since 316L was first printed by Kruth in 2003 [21], most research has focused on tensile and HCF (high cycle fatigue) behavior and properties. In terms of tensile properties, 316L can achieve an excellent balance between strength and ductility through SLM technology [22]. The high strength of SLM 316L is attributed to the fine sub-structure [23], high dislocation density [24], very low-angle grain boundaries [25], and dispersive nano-oxides [26] formed by the high process cooling rates. However, anisotropy, hierarchical features and defects of SLM 316L have a significant influence on fatigue property. Firstly, SLM 316L has anisotropic properties due to grain growth along the build direction. Wood et al. [27] investigated the influence of build orientation on fatigue strength, and found that horizontally-printed specimens have 20%-45% higher fatigue strength than vertically-printed specimens due to

the higher tensile strength and smaller surface roughness of the former. Stern et al. [28] reached a similar conclusion that vertically printed specimens have weak bonding between layers and lower resistance to crack growth. The loading direction, which in turn depends on the build direction, affects crack growth path and rate [29, 30]. In addition, different effective areas of defects in various loading direction would affects fatigue properties [28]. Secondly, the hierarchical feature of SLM 316L has a significant influence on fatigue performance. Hatami et al.[31] discovered that layer thickness has a minor negative impact on fatigue strength, however it has a significant effect on the production efficiency. Also, the direction and thickness of layers affect crack growth paths and rates [29, 30]. Thirdly, defects, which are a dominant feature of SLM 316L, have an adverse influence on fatigue properties. Defects in SLM can be divided into surface and internal defects. Surface defects are mainly surface roughness and surface pores. As many previous studies have shown, specimens after machining [27, 31, 32] or electropolishing [33, 34] have significantly higher fatigue properties than as-built specimens because surface pores have a significant detrimental effect on HCF strength [35]. Regarding internal defects, including key holes, gas pores, and lack of fusion, among which lack of fusion is more dangerous for fatigue loading due to its large volume and sharp shape. Compared with internal defects in the core, internal defects in the sub-surface have a larger effect on fatigue strength and life cycles [35-37]. Hence, various methods of process parameter optimization and post heat treatment, like annealing and hot isostatic pressing, have been developed for reducing internal defects or increasing defect tolerance [38]. To date, little research has been conducted on deformation mechanisms of additively manufactured stainless steel. Zhang et al. [39] demonstrated that HCF loading promotes local recrystallization of SLM 304L at room temperature. The recrystallization behavior, in turn, in the overlap area, has a detrimental effect on fatigue performance by weakening resistance to fatigue crack initiation. For LCF loading at room temperature, twin boundaries act as sites for crack initiation in SLM 304L [40]. Most studies on fatigue of SLM material are focused on HCF behavior at room temperature. To the authors' knowledge, little research has been presented on deformation mechanisms and LCF behavior for SLM 316L at high temperature.

In the present study, the tensile properties and microstructure of SLM 316L are investigated by means of tensile tests and EBSD (Electron Backscattered Diffraction) analysis. In addition, a series of LCF tests at various strain amplitudes is conducted on SLM 316L and traditional 316L to examine the comparative performance. Through analysis of cyclic stress response, hysteresis loops, and plastic strain energy, the cyclic deformation behavior of SLM 316L is characterized. Furthermore, the specific cyclic softening behavior of SLM 316L is investigated from the aspect of microstructure evolution. In addition, the influence of the strain amplitude on the development and propagation of fatigue cracks is examined. Finally, a life prediction model based on non-Masing behavior is

developed to predict the LCF life of SLM 316L. The overall objective of the work is to characterize the LCF properties and corresponding deformation mechanisms of SLM 316L under different strain amplitudes.

2. Experimental details

2.1 Materials

The investigated SLM specimens are fabricated in a 99.999% argon atmosphere by SLM 125HL (SLM Solutions GP, Germany) equipped with a 400 W fiber laser, using commercial standard process parameters. The following process parameters are used: laser power (P) = 200 W, scanning speed (V) = 800 mm/s, layer thickness (t) = 30 μm, hatch distance (H) = 120 μm, pre-heat temperature (T_{pr}) = 100 ℃. The gas-atomized powder size is distributed from 10 to 45 μm, and its nominal chemical composition (in wt.%) is shown in Table 1. By using Archimedes method, the relative density of the SLM 316L was found to be greater than 99.3%, which meets the ASTM F3184-16 standard [41]. It should be mentioned that the final tested specimens are machined and polished from blocks as shown in Fig. 1. Before the fatigue tests, the surface of the specimen gauge length is polished to Ra < 0.2 μm, to make sure that no visible defects exist and the surface condition does not affect the fatigue results. To identify the differences between SLM and traditional 316L, the latter specimens were also machined to the same surface condition. The traditional 316L material is cut from cold-drawing 316L pipe and is solution treated at 1040 ℃ for 2h in air, followed by water quenching. Fig. 1(b) illustrates the geometry of the test specimen and Table 1 lists the chemical compositions for SLM 316L and traditional 316L. In order to investigate the individual influence of fatigue loading and thermal aging on microstructure of SLM 316L during LCF tests, a sample without loading is put in furnace for long-time aging at 550℃.

Table 1 Chemical compositions of materials (wt.%)

	Fe	Cr	Ni	Mo	Mn	Si	P	S	C	N
316L powder	Balance	16-18	10-14	2-3	2.00	1.00	0.045	0.03	0.03	0.100
SLM 316L	Balance	18.46	12.49	2.4	0.74	0.75	0.025	0.012	0.040	0.054
Traditional 316L	Balance	18.07	11.78	2.29	1.12	0.41	0.032	0.0071	0.034	0.031

2.2 Microstructural characterization

To further reveal microstructural features, the specimens are ground by 2000 grits silicon carbide abrasive paper and polished using 3 μm diamond suspension, followed by electrolytic etching using saturated oxalic acid, applying 0.09 A/cm^2 for 45 s at room temperature. The microstructure characterization is carried out by Optical Microscope (OM) and Scanning Electron Microscope (SEM) with Electron Backscattered Diffraction (EBSD) system. In order to investigate the change of cellular sub-structure, at least 10 micrographs are used to calculate the diameter of the cellular structure. Grain orientation and qualitative analysis of the GND density distribution are

performed by EBSD mapping with a step size of 500 nm under an accelerating voltage of 20 kV, using an Oxford Symmetry detector. The EBSD maps were obtained using Aztec data acquisition software at step sizes of 500 nm. The EBSD data is further analyzed with HKL Channel 5 software and the MTEX MATLAB toolbox [42, 43]. The GND mapping and density are calculated based on Pantleon's theory [44], which has been successfully applied to other alloys and SLM 316L to quantify GND density distribution [42, 43, 45]. A 10° misorientation criterion was used to distinguish low angle grain boundaries (LAGB) and high angle grain boundaries (HAGB).

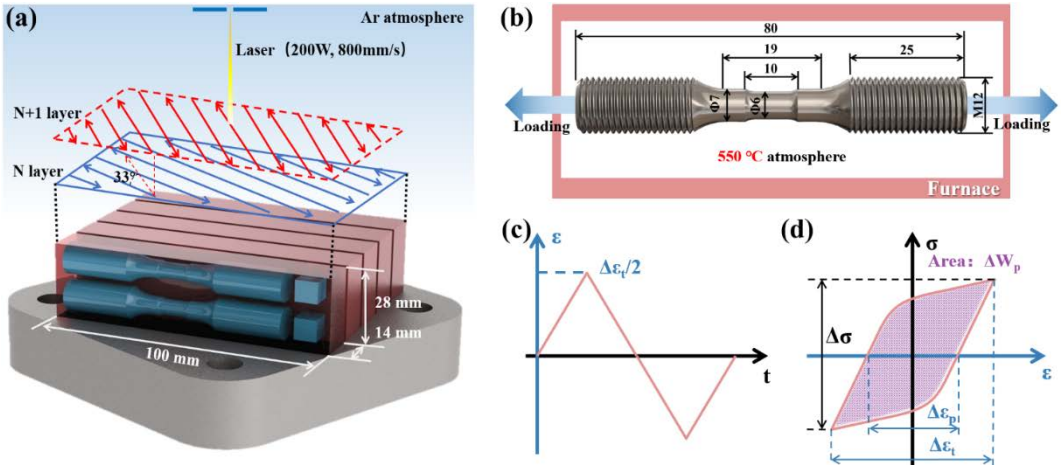

Fig. 1 (a) Schematic of scanning strategy and specimen position; (b) definition of specimen geometry; (c) loading wave-form; (d) definition of related parameters.

2.3 Tensile and fatigue tests

Room-temperature uniaxial tensile tests were conducted at a strain rate of 1.0×10^{-3} s^{-1}. The gauge length is 10mm. The LCF tests were conducted using SINOTEST EQUIPMENT RPL-100 fatigue test machine equipped with an elevated temperature furnace. A series of fully-reversed axial strain-control tests was performed with a constant strain rate of $1.0\times10^{-3}s^{-1}$ at 550 ℃, for strain amplitudes of 0.3%, 0.4%, 0.6%, 0.8% and 1.0%. The temperature was measured by three K-type thermocouples near the gauge section. A 10 mm gauge extensometer produced by Epsilon was used to measure the deformation. All experimental data (stress, strain, time, etc.) are collected by EDC220 controller according to the specified time interval.

Commonly, strain-controlled fatigue tests are stopped before final fracture to avoid extensometer damage due to sudden (uncontrolled) fracture. This leads to the adoption of different end-of-test (failure) criteria and hence failure cycles for different materials. For example, Totemeier et al. [46] used 20% "stress ratio" (Peak tensile stress/Peak compressive stress) reduction from the point of crack initiation as the failure criterion for INCONEL 617. Zhang et al. [47] used a 10% drop in peak stress from the stable softening stage as the fatigue life for P92 steel. Kim et al. [48] defined a 20% reduction of the maximum stress as the fatigue lifetime for 316L and 316LN materials.

In order to appropriately define a unified failure criterion for SLM 316L and traditional 316L, a new life end criterion is adopted here, as described in Fig.2 (a) and (e). It can be seen that “cusp” appears on the compression stage for a σ_{max} drop of between 25% and 30%, which indicates the initiation of a macrocrack as shown in Fig.2 (c), (d), (g) and (h) [49]. Hence, to avoid such macrocracks during service, a σ_{max} drop of 25% is adopted here as the criterion for initiation of a macrocrack and, hence, as a failure criterion. So, the cycle number corresponding to a drop of 25% maximum peak stress is defined as the fatigue life for SLM 316L and traditional 316L.

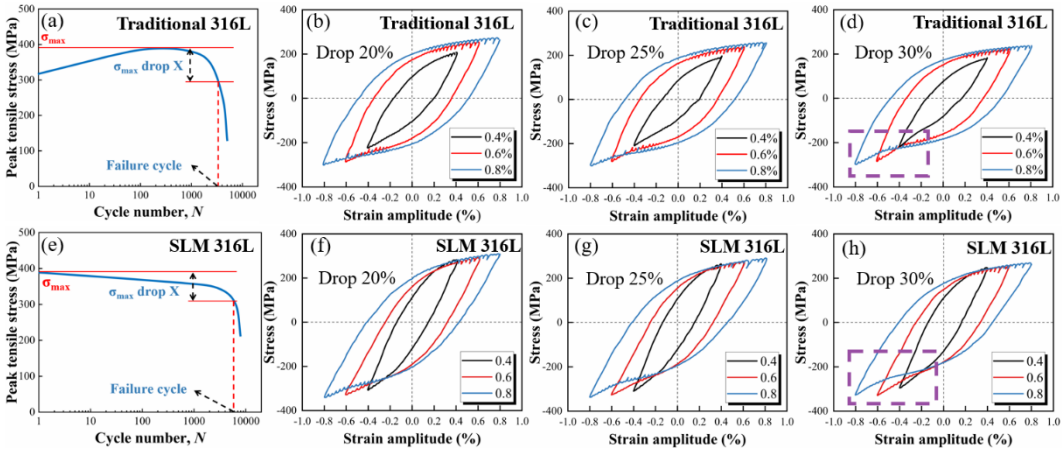

Fig. 2 The curves of peak tensile stress of (a) traditional 316L and (e) SLM 316L, and the stress-strain hysteresis loop at different σ_{max} drops (20%, 25%, 30%) of (b-d) traditional 316L; (f-h) SLM 316L (purple box indicate “cusp”).

3. Experimental results

3.1 Microstructural characterization

Fig. 3(a) shows the representative microstructure in SLM 316L. As shown in Fig. 3(a), SLM 316L has a hierarchical and finger-shaped formation due to the layer-by-layer and track-by-track melting method. The melt pool boundaries (red line in Fig. 3(a)) are attributed to the laser track and the powder layer. Its width and depth are dependent on laser diameter and thickness of the powder layer, respectively. The area surrounded by the blue line is the remelt zone which is intersected by two adjacent melt pools in the same layer. From Fig. 3(a), a very fine sub-structure is observed within the melt pool. The sub-structure has two shapes of columnar and cellular structures from different views.

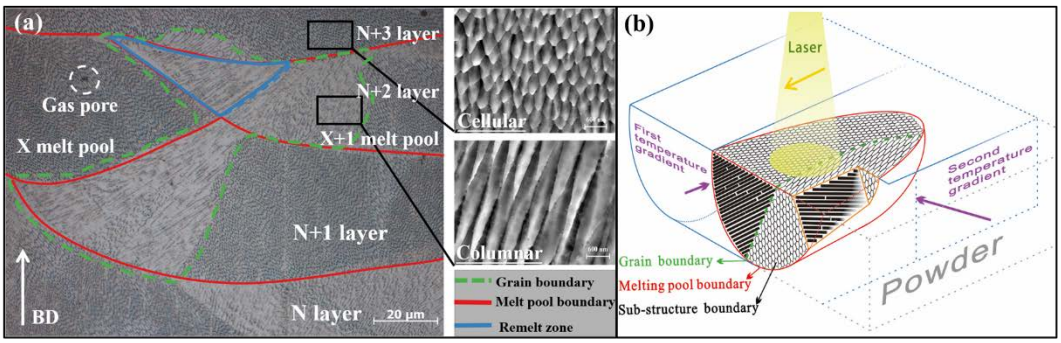

Fig.3 (a) Microstructure of SLM 316L (BD: build direction); (b) The schematic of cellular sub-structure growth.

Fig.4 displays a representative grain orientation map and misorientation angle distribution for SLM 316L in as-built condition. It is observed that many columnar and complex grains are distributed in SLM 316L. The grains grow along the build direction, which corresponds to the temperature gradient between layers. The melt pool boundary and powder layer can't be observed in the EBSD map, indicating that the melt pool boundary and powder layer have no obvious influence on the growth of grains and sub-structure. In addition, the cellular sub-structure cannot be identified from the EBSD orientation map, proving that the cellular sub-structure has same crystallographic orientation. From Fig. 4(b), it can be seen that SLM 316L has a large fraction (about 79%) of LAGB, with misorientation less than 10°.

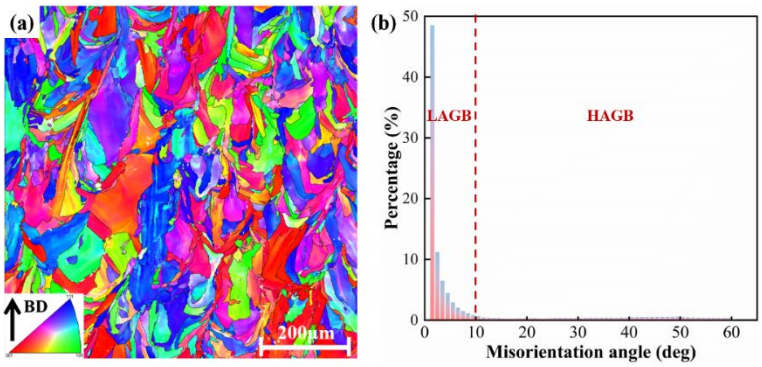

Fig. 4 EBSD analysis of SLM 316L: (a) Grain orientation map; (b) histogram of misorientation angle distribution.

3.2 Tensile properties

Fig. 5 shows the measured engineering stress-strain curves of both SLM 316L and traditional 316L, and the tensile properties results of 0.2% offset yield strength (YS), ultimate tensile strength (UTS) and elongation are listed in Table 2 with additional comparative data. The stress-strain curve of the traditional 316L exhibits a quite wide region of work hardening after yielding (289 MPa) until the UTS (589 MPa) is reached at the maximum uniform elongation (UE) of ～62%. The tensile stress then drops till fracture occurs at a tensile elongation of ～92%. The YS of SLM 316L is 568 MPa, which is 96.5% higher than that of traditional 316L. After yielding, the tensile stress reaches the UTS rapidly with a narrow region of work hardening. The 52% elongation of SLM 316L is much lower

than 93% elongation of traditional 316L, is still higher than the standard value 35% for wrought material.

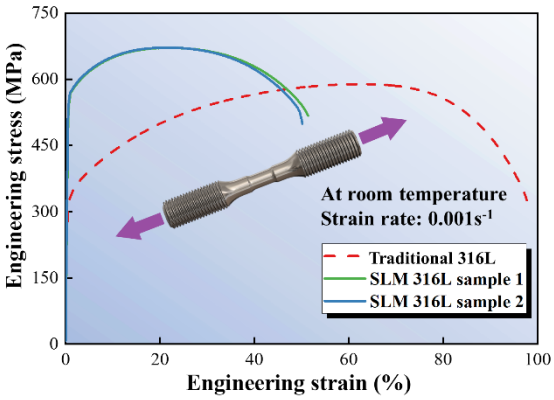

Fig. 5 Measured stress-strain curves of SLM 316L and traditional 316L.

Table 2 Tensile properties of different materials.

Material	YS (MPa)	UTS (MPa)	Elongation (%)	Source
Traditional	289	589	93	This work
SLM	568	693	52	This work
Wrought	~300	~620	~65	[50, 51]
Standard for wrought	≥170	≥485	≥35	ASTM A312 [52]

3.3 Fatigue properties

As is shown in Fig. 6, SLM 316L exhibits a typical cyclic softening behavior at different strain amplitudes, whereas, in contrast, traditional 316L exhibits cyclic hardening behavior. In traditional 316L, the material shows initial hardening, saturation and rapid softening. The degree of hardening is found to be dependent on strain amplitude, increasing with strain amplitude. Compared with the rapid increase and decrease of peak tensile stress in traditional 316L, SLM 316L has a more stable cyclic behavior, which is beneficial for engineering applications. It is noting that SLM 316L exhibit initial cyclic hardening in few cycles at 0.8% and 1.0% strain amplitude.

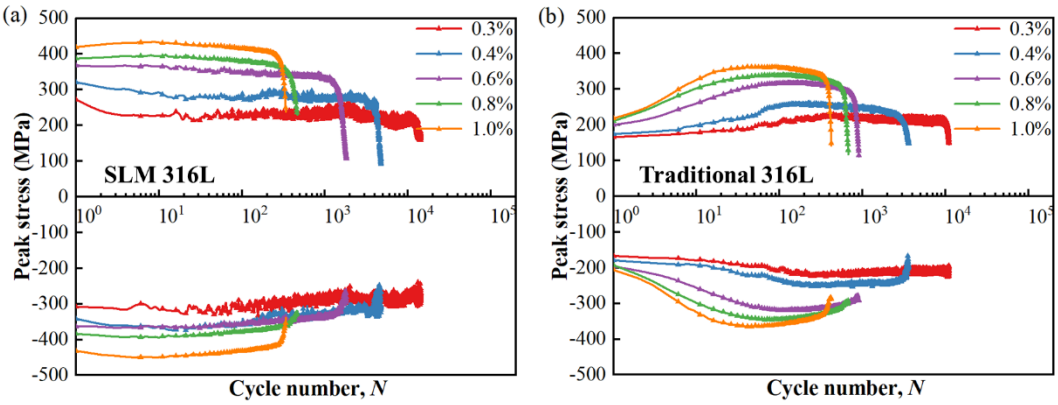

Fig.6 Peak stress curves of (a) SLM 316L and (b) traditional 316L at different strain amplitudes.

From Fig.6 (a) and (b), the strain amplitude is seen to have a significant influence on fatigue life. The fatigue life data for all tests in the present work is listed in Table 3. Fatigue life decreases with increasing strain amplitude

in both SLM 316L and traditional 316L. Compared with traditional 316L, SLM 316L has significantly longer fatigue life at strain amplitudes of 0.3, 0.4, 0.6%, although traditional 316L has slightly better performance at 0.8 and 1.0% amplitudes. However, SLM 316L has a much higher stress amplitude than traditional 316L, indicating higher cyclic strength. Hence, SLM 316L has better LCF properties at 0.3, 0.4, 0.6% strain amplitudes and similar LCF properties at 0.8, 1.0% strain amplitudes, considering the same roughness and no surface defect.

Table 3 Fatigue life of SLM 316L and traditional 316L.

Temperature (℃)	Material	Total strain amplitude, $\Delta\varepsilon_t/2$ (%)	Fatigue life, N_f (cycles)
550	SLM 316L	0.3	12450
550	SLM 316L	0.4	4017
550	SLM 316L	0.6	1513
550	SLM 316L	0.8	433
550	SLM 316L	1.0	392
550	Traditional 316L	0.3	10857
550	Traditional 316L	0.4	3300
550	Traditional 316L	0.6	832
550	Traditional 316L	0.8	618
550	Traditional 316L	1.0	398

The total strain amplitude is the summation of the plastic strain amplitude and elastic strain amplitude, combining the Coffin-Manson and Basquin relationships [53]:

$$\frac{\Delta\varepsilon_t}{2}=\frac{\Delta\varepsilon_e}{2}+\frac{\Delta\varepsilon_p}{2}=\frac{\sigma'_f}{E}(2N_f)^b+\varepsilon'_f(2N_f)^c \quad (1)$$

where $\Delta\varepsilon_t/2$ is the total strain amplitude, $\Delta\varepsilon_e/2$ and $\Delta\varepsilon_p/2$ are the elastic strain amplitude and the plastic strain amplitude, respectively. The constant σ'_f is the fatigue strength coefficient and *b* is the fatigue strength exponent, obtained from the intercept and slope of linear fitting between $\log(\Delta\varepsilon_e/2)$ versus $\log(2N_f)$. Similarly, ε'_f is the fatigue ductility coefficient and *c* is the fatigue ductility exponent, obtained from the intercept and slope of linear fitting between $\log(\Delta\varepsilon_p/2)$ versus $\log(2N_f)$. The fatigue parameters of traditional and SLM 316L are listed in Table 4.

Table 4 Fatigue parameters of SLM 316L and traditional 316L.

	σ'_f	*b*	ε'_f	*c*	*K'*	*n'*
SLM 316L	1125.45	-0.16	0.28	-0.61	926.83	0.17
Traditional 316L	1309.65	-0.17	0.18	-0.74	491.05	0.30

As shown in Fig.7 (a), the strain amplitude and fatigue life cycles can be described accurately with the Coffin-Manson and Basquin relationships, which is beneficial for life prediction in SLM 316L. The transitional fatigue cycle is defined as transitional fatigue life (N_T) where elastic strain amplitude equals plastic strain amplitude. Plastic strain amplitude has a dominant effect on fatigue life when total strain amplitude is greater than the transition point.

The higher strength and lower ductility characteristics of SLM 316L offer longer fatigue life than traditional 316L under lower strain amplitudes e.g. (<0.8 %) and shorter fatigue life under higher strain amplitude. In contrast, Fig.7 (b) indicates that, for traditional 316L, plastic deformation predominates fatigue life when strain amplitudes are larger than about 0.4%. This can be attributed to the lower strength and higher ductility compared to the SLM material, as shown in Fig. 5.

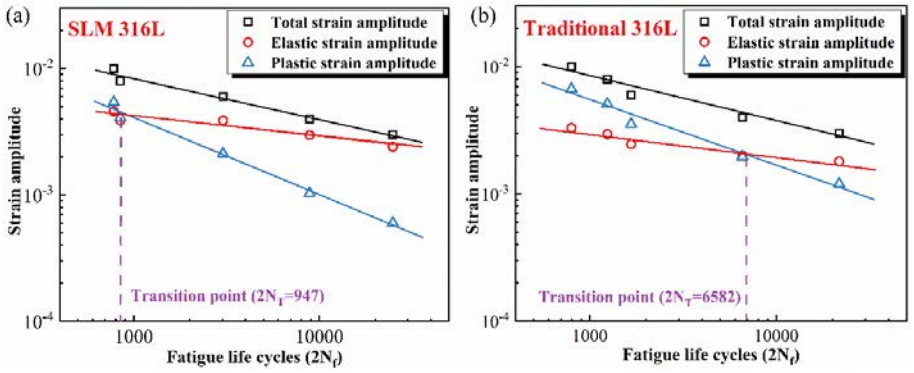

Fig.7 Relationship between strain amplitudes and fatigue life cycles：(a) SLM 316L; (b) Traditional 316L.

3.4 Crack propagation and fracture morphology

The gauge length is cut longitudinally to observe the crack nucleation and propagation path after LCF tests. Fig. 8(a-c) shows typical transgranular cracks under different amplitudes in traditional 316L. The fatigue cracks originate from the surface and subsequently propagate into the core of the specimens. As is shown in Fig. 8(g), for lower strain amplitudes, e.g. 0.4 %, most plastic deformation is concentrated in a persistent slip band and a crack is nucleated at the intersection of the surface and a slip band. Fig. 8(h) shows that the grain boundary near the surface is torn open and a crack nucleates due to larger plastic deformation when the strain is higher (0.8%). There are many long and thin cracks near the fracture surface at 0.4% strain amplitude, because these cracks have enough time to nucleate and propagate. In contrast, at 0.8% strain amplitude, cracks are fewer and straighter, contributing to larger plastic deformation and shorter life. Generally, the higher the strain amplitude, the fewer and shorter the fatigue cracks.

Similarly, transgranular fracture is observed in SLM 316L at different strain amplitudes. Fig. 8(d-f) shows that columnar grains are widely distributed in SLM 316L. The cracks originate from the surface and propagate into the core of the specimens. The crack initiation locations seem to be randomly distributed on the surface. Strain amplitude has a significant influence on crack length. At higher strain amplitudes, shorter cracks are observed. In addition, the melt pool boundary appears to have no obvious effect on crack propagation.

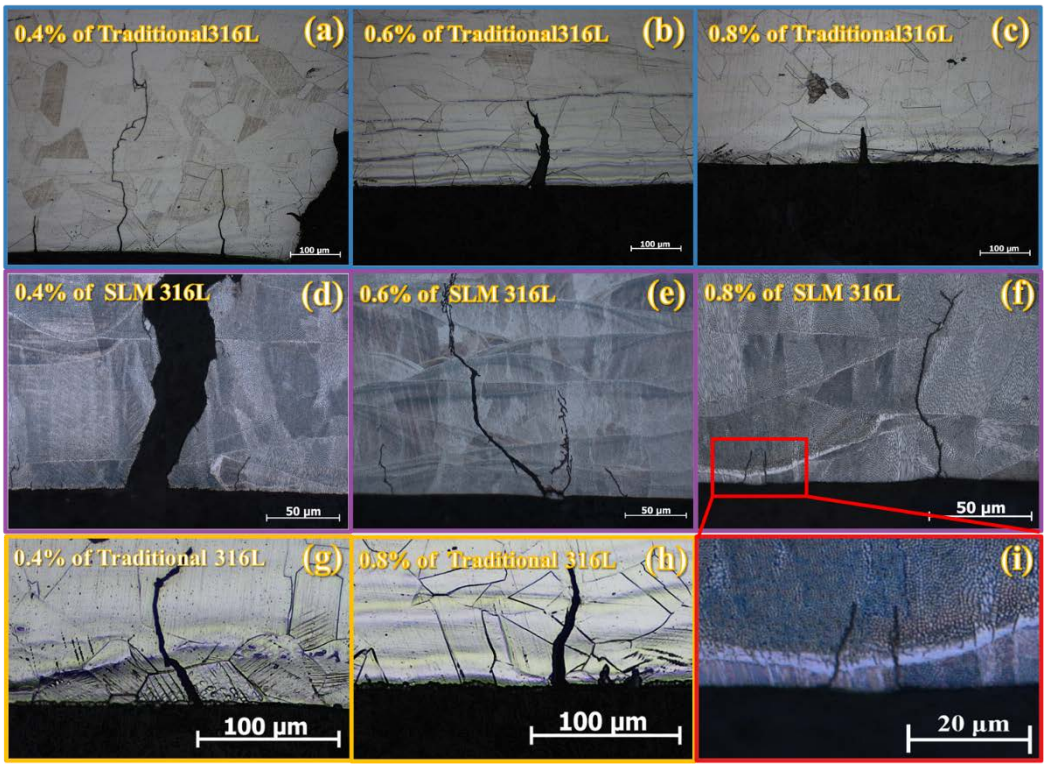

Fig.8 Crack path in the vicinity of fracture surface: (a-c) traditional 316L at 0.4, 0.6, 0.8% strain amplitude; (d-f) SLM 316L at 0.4, 0.6, 0.8% strain amplitude; (g) crack originated at the intersection of surface and a slip band; (h) crack originated at the grain boundary; (i) the crack paths across the melting boundary.

Three representative specimens after LCF tests at strain amplitudes of 0.4%, 0.6%, and 0.8% are chosen for investigation of the morphology of fracture surface, the SEM images of which are shown in Fig. 9. The fracture morphology includes three regions: (ⅰ) fatigue crack initiation site, (ⅱ) crack growth region, and (ⅲ) rupture region. The fatigue crack initiation sites and crack growth regions are characterized by a radial flow pattern, whereas the final fracture zone exhibits typical ductile fracture. As shown, the numbers of fatigue crack initiation sites are 5, 2, and 1 for the 0.4%, 0.6%, and 0.8% cases, respectively. With increase in strain amplitude, the number of crack initiation sites decreases. This is consistent with the results of the OM analysis. From the fracture, lack-of-fusion defects are observed near the surface. As is shown in Fig. 9(e)(f)(h)(i)(k)(l), the fatigue cracks initiate from the lack-of-fusion defects near the surface at 0.4, 0.6 and 0.8%strain amplitudes. When strain amplitude is 0.4%, a closer observation shows that the crack also initiates from the sub-surface of the oxide layer (Fig. 9(b), (c)). The figure with a green border in Fig. 9(d) clearly shows many striations and fine oxide particles adhere to the fatigue striations at 0.4% strain amplitude. The oxidation effect can't be ignored during fatigue crack propagation. As is shown in Fig. 9(m-o), secondary cracks can be observed during the propagation of fatigue cracks.

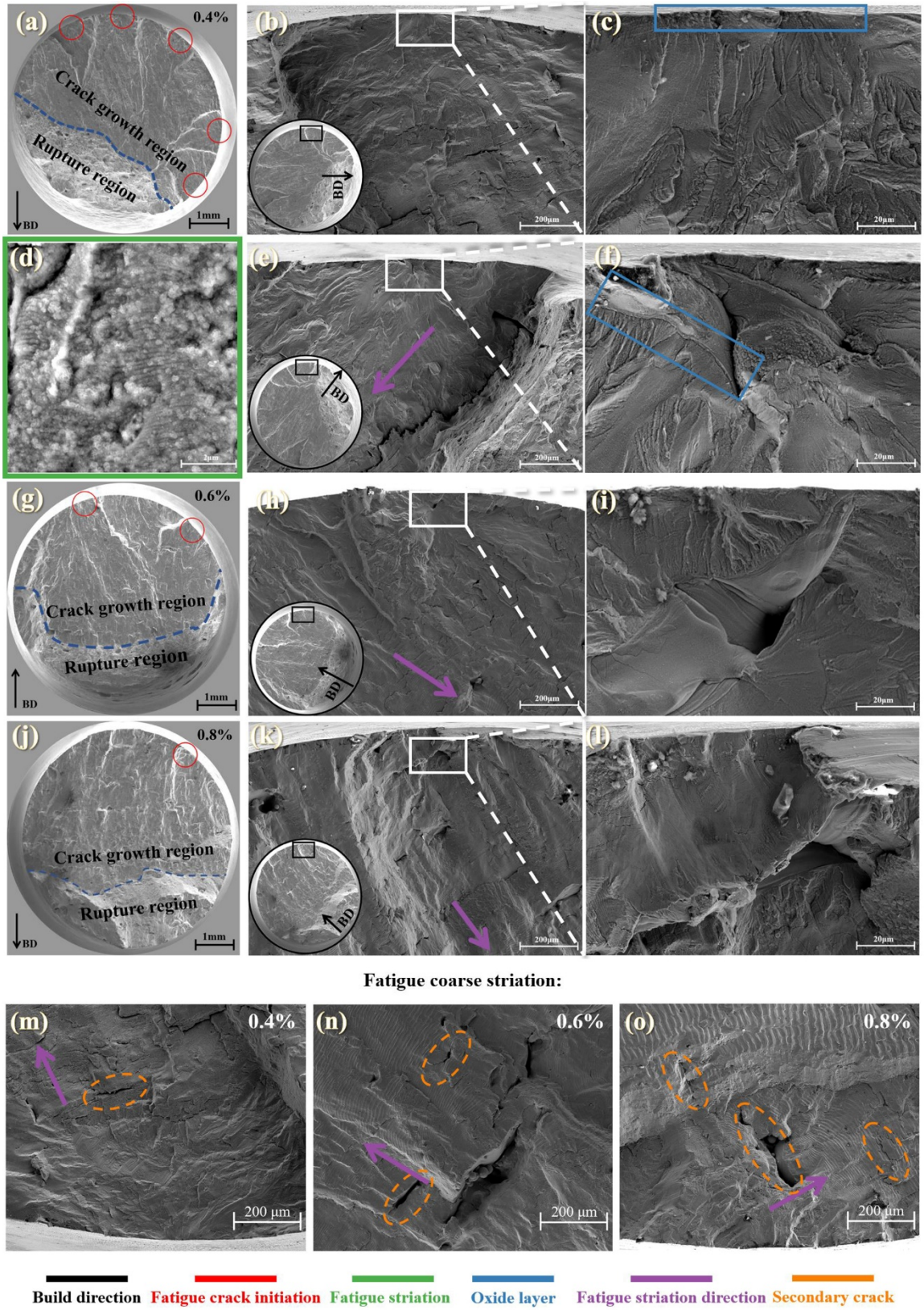

Fig.9 The fracture morphology of SLM 316L: (a-c, e-f) 0.4%; (d) oxide characterization of 0.4% LCF; (g-i) 0.6% LCF; (j-l) 0.8% LCF; (m-o) secondary crack and fatigue striation direction of 0.4, 0.6, and 0.8% respectively.

4.Disscusssion

4.1 Microstructural analysis

As is shown in Fig .3(a), the sub-structure is widely distributed in the grains. The sub-structure is attributed to dendritic segregation in the melt pool due to the very high cooling rate [23]. As shown in Fig. 3(b), the high cooling rate leads to cellular (or columnar) solidification and cellular substructure growth along the temperature gradient [54]. The first temperature gradient from the last cooled melt pool makes a cellular sub-structure grow at about 45° to the direction of build. The second temperature gradient leads a growth of a cellular sub-structure along the laser scanning direction. So, the cellular and columnar shapes can be seen in the melt pool, both referred to as “cellular sub-structure”. Between adjacent layers, the melt pool boundary does not prevent growth of the cellular substructure (green lines in Fig. 3(a)). In addition, the walls of the cellular sub-structure with high dislocation density play an important role in the grain boundary strengthening for improved strength [6]. From Fig. 3(a), the diameter of the cellular sub-structure is 0.73 ± 0.064 μm after statistical analysis. The fine cellular sub-structure can bring high strength for SLM 316L. After misorientation analysis, SLM 316L has a large fraction (about 79%) of LAGB. The large number of LAGBs is also a key factor for the high strength of SLM 316L, which has been reported by Wang et al [22].

4.2 Fatigue behavior

4.2.1 Degree of softening

From Fig.6 (a), the strain amplitude is seen to have an obvious effect on cyclic softening behavior of SLM 316L. Fig. 10(a) shows the evolution of the degree of softening (DOS) to quantify the softening variation with increasing strain, with DOS defined as follows:

$$DOS = \frac{\sigma_a^1 - \sigma_a^{half}}{\sigma_a^1} \tag{2}$$

where σ_a^1 and σ_a^{half} are the peak tensile stresses of the first and half-life cycles, respectively. It is clear that DOS decreases as strain amplitude increases. However, some studies show that higher strain amplitude gives higher softening [53, 55], which is contrary to the observed phenomena in this study. The softening behavior in SLM 316L will be further discussed below in Section 4.3 below.

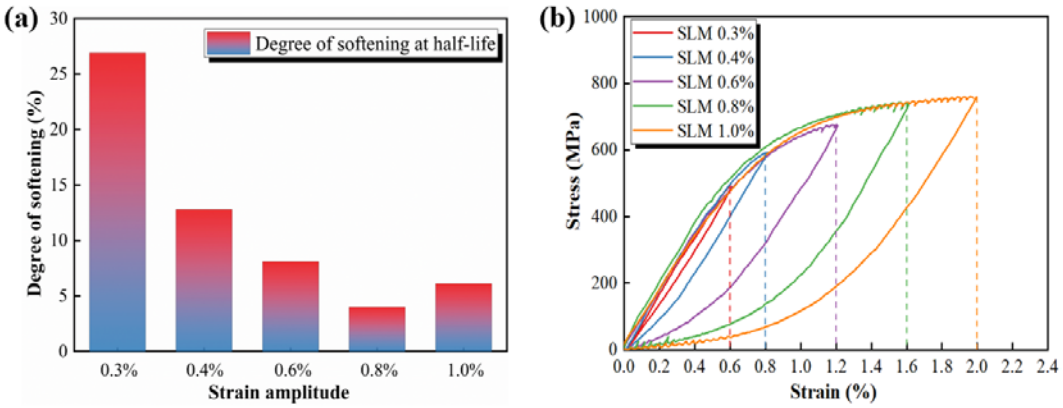

Fig. 10 (a) Evolution of degree of softening; (b) Stable hysteresis loops with matched lower tips in SLM 316L.

4.2.2 Cyclic deformation behavior

The Ramberg-Osgood relationship is used to describe the correlation between stress amplitude $\Delta\sigma/2$ and plastic strain amplitude $\Delta\varepsilon_p/2$, as follows:

$$\frac{\Delta\sigma}{2} = K'\left(\frac{\Delta\varepsilon_p}{2}\right)^{n'} \tag{3}$$

where *K'* is cyclic strain hardening coefficient and *n'* is the cyclic strain hardening exponent. The relevant parameters are also determined from the stabilized hysteresis loops at half-life under different strain amplitudes, as listed in Table 4.

Further, the origin of the coordinate axes is transformed to the tip of the compressive cycle shown in Fig.10. If the loading curves of the hysteresis loops could overlap precisely, the material can be considered as Masing material. Generally, the basic assumption in Masing behavior is that the deformation structure remains the same irrespective of the strain amplitudes [56]. However, the hysteresis loops are not found to follow the common loading curve and depicts the non-Masing behavior, as is shown in Fig.10(b). The non-Masing behavior of SLM 316L is attributable to microstructure instability [57] under LCF loading conditions, which will be discussed in Section 4.3.

The variation of plastic strain energy (ΔW_p, the area in the hysteresis loop, as shown in Fig.1 (d)) characterizes the damage in the material. ΔW_p follows the general relationship:

$$\Delta W_p \propto \Delta\sigma\Delta\varepsilon_p \tag{4}$$

Fig. 11 shows the evolution of plastic strain energy for different strain amplitudes. In SLM 316L, ΔW_p is relatively stable below 0.3% and 0.4% amplitudes, which is beneficial for life prediction. Peak stress decreases and plastic strain amplitude increases with cycling. There is a sudden decrease in the final few cycles for 0.6, 0.8 and 1.0% strain amplitudes. The rate of decrease in stress is greater than that of increase in plastic strain amplitude due to micro-crack initiation. As shown in Fig. 11(b), the plastic strain energy for traditional 316L increases and decreases much more rapidly than SLM 316L at different strain amplitudes, consistent with its rapid cyclic hardening behavior.

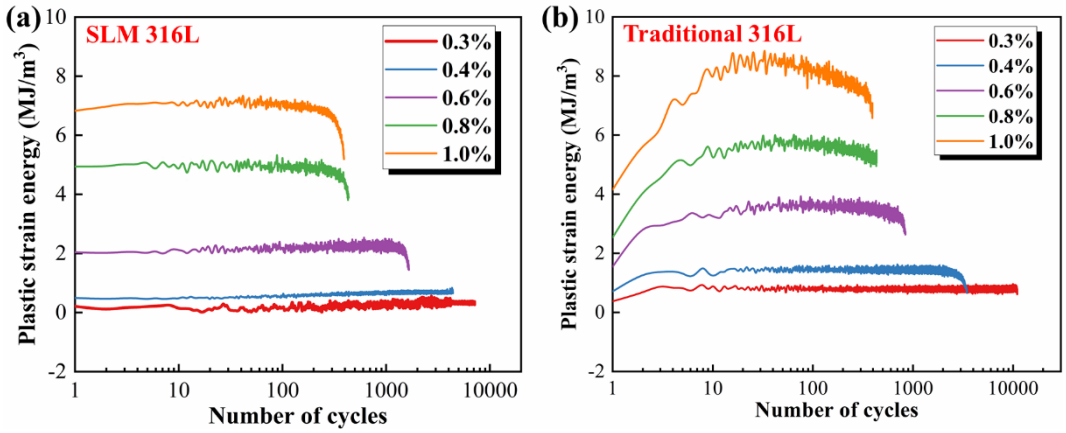

Fig. 11 The evolution of plastic strain energy in (a) SLM 316L and (b) traditional 316L.

4.3 Microstructural evolution

Fig. 12(a) shows the evolutions of elastic strain amplitude and the yield stress ($\sigma_{0.2}$) of 1.0% LCF tested sample. During the fatigue life, the elastic strain amplitude decreases continuously under different strain amplitudes, indicating that the SLM 316L would yield at lower strain. In addition, the elastic modulus decreases generally during the fatigue life shown in Fig. 12(b). The decreases of elastic strain and elastic modulus collectively lead to the gradual decrease of yield stress (brown dots shown in Fig. 12(a)) with the fatigue cycles. The decrease of yield stress contributes to the cyclic softening in the cyclic deformation behavior of SLM 316L. The mechanisms responsible for the reduction of yield stress under fatigue loading will be discussed in more detail in the following section.

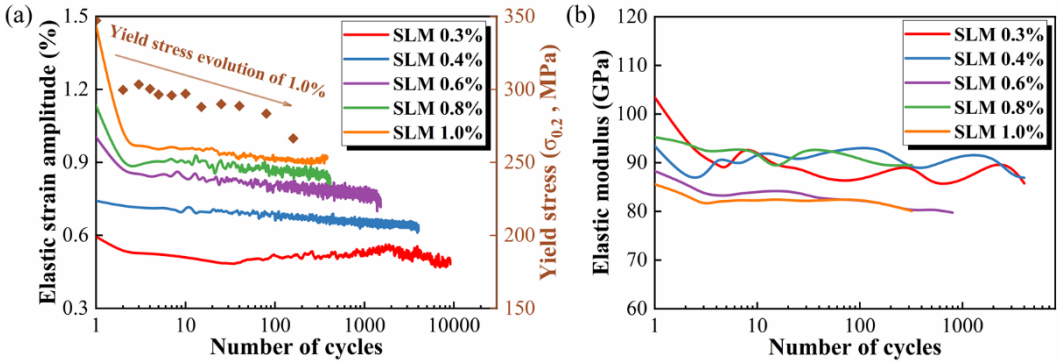

Fig.12 The evolution of (a) elastic strain amplitude under different amplitudes (the brown dots indicate the yield stress evolution of 1.0% LCF tested sample); (b) elastic modulus under different amplitudes.

4.3.1 Cellular sub-structure

Fig. 13 shows the coarsening of the cellular sub-structure after fatigue loading and high-temperature aging. As mentioned above, the cellular sub-structure is the key factor for improving the strength of SLM 316L [22]. The evolution of the cellular sub-structure therefore can be expected to affect the cyclic deformation behavior under

LCF conditions. From the OM images, the diameter of cellular structure in as-built SLM 316L is 0.707 ± 0.078 μm, which is in agreement with published data [23, 58]. As shown in Fig. 13, the size of the sub-structure is 0.709 ± 0.039 μm after aging at 550℃ for 325 h. This indicates that the sub-structure has excellent thermal stability at the high temperature of 550℃. This can be attributed to the enrichment of Cr and Mo in the cellular structure walls [58]. However, fatigue loading has a significant influence on the cellular sub-structure. The diameter of the cellular sub-structure grows to 0.73 ± 0.064 μm, 0.75 ± 0.061 μm and 0.82 ± 0.087 μm after 0.4%, 0.6% and 0.8% strain amplitude respectively.

This sub-structure coarsening leads to cyclic softening. Pham et al. [23] identified a Hall-Petch relationship between yield strength and size of sub-structure. So, sub-structure coarsening directly leads to decrease of yield stress during fatigue loading, obviously causing the cyclic softening in SLM 316L.

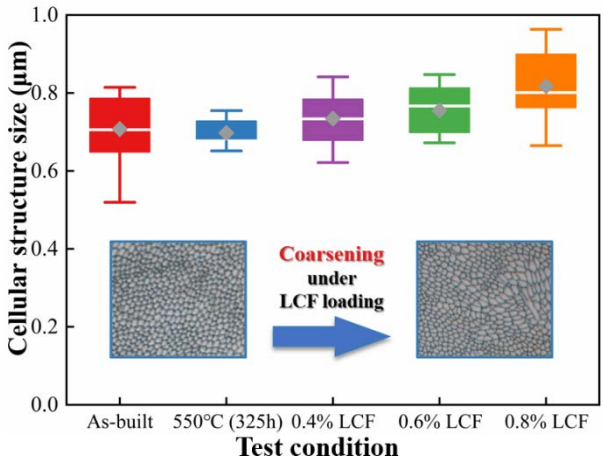

Fig. 13 The evolution of cellular sub-structure in different conditions.

4.3.2 Crystal texture

Fig. 14(a-c) show the grain orientations of the as-built, 0.4% and 0.8% fatigued samples. Fig. 14(d-f) are inverse pole figures which used Exp. Densities to reflect the distribution frequency of grain orientations in the analyzed areas. Fig. 14(d-f) show obvious concentration of grain orientations and exhibit obviously different textures along the loading direction (LD) in as-built and post-test fatigue samples. It is noticeable from Fig. 14(a) that the microstructure consists of a mixture of fine, coarsen and columnar grains. The columnar grains are generally parallel to the build direction. So, the as-built samples shows ＜111＞ ∥ LD and ＜001＞ ∥ LD texture in Fig. 14(d). From Fig. 14(e-f), the ＜111＞ ∥ LD disappeared, and the intensity of ＜001＞ ∥ LD increased with the increasing of strain amplitude. So, it is concluded that the ＜111＞ ∥ LD texture transforms into ＜001＞ ∥ LD texture after cyclic LCF loading. For FCC (face-centered cubic) materials, texture direction directly influences tensile properties. Compared with ＜111＞ ∥ LD texture, ＜001＞ ∥ LD texture has lower yield stress and elongation due to different

Schmid factors [59]. And, the maximum value of the elastic modulus of FCC is obtained along the ＜111＞ direction and the minimum along ＜001＞ direction [60]. The elastic modulus evolution shown in Fig. 12(b) is also attributed to the gradual texture evolution. In summary, the texture evolution from ＜111＞∥LD to ＜001＞∥LD leads to the decreasing of yield stress and elastic modulus during cyclic loading in SLM 316L.

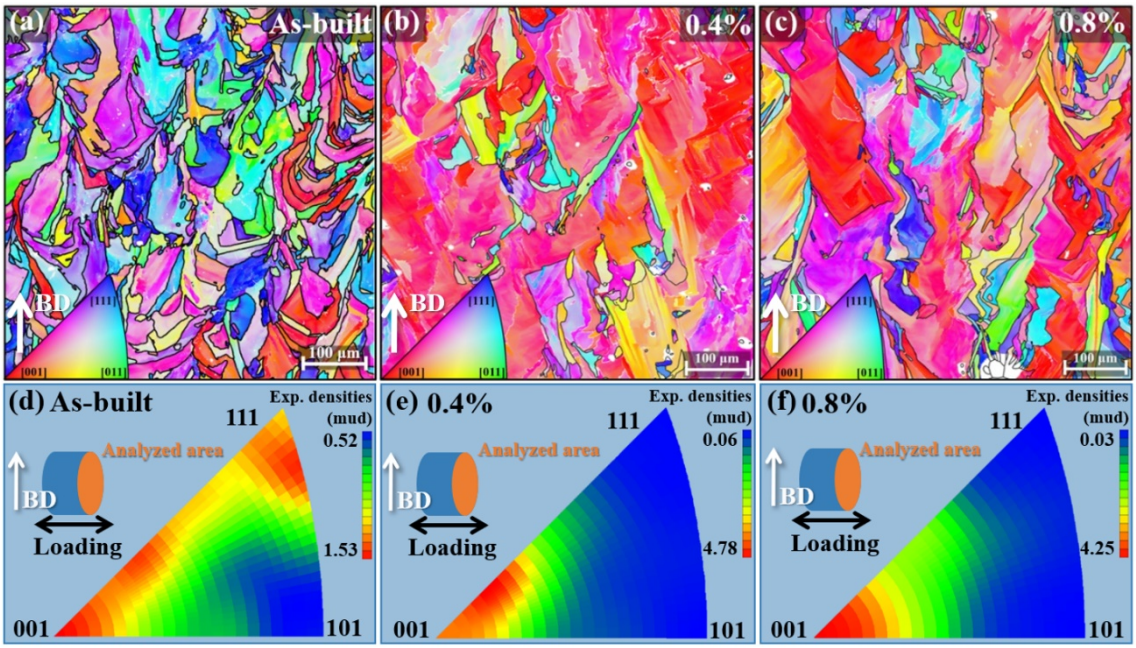

Fig. 14 EBSD inverse pole figure (IPF) orientation maps of (a) as-built, (b) 0.4% LCF, and (c) 0.8% LCF; Inverse pole figure (IPF) of (d) as-built, (e) 0.4% LCF, and (f) 0.8% LCF.

4.3.3 Geometrically necessary dislocations and low angle grain boundary

Fig. 15 shows the GND density maps within the selected area of 300×200 μm indicated from EBSD-acquired data for the as-built and post-fatigue samples. The GND is heterogeneously distributed. The average density of GND is $7.54\times10^{14}/m^2$ for as-built SLM 316L. After the cyclic loading at the strain amplitudes of 0.4 and 0.8%, the GND densities reduce to $4.89\times10^{14}/m^2$ and $4.48\times10^{14}/m^2$ respectively. As a result, the stress required for dislocation movement decreased, leading to cyclic softening.

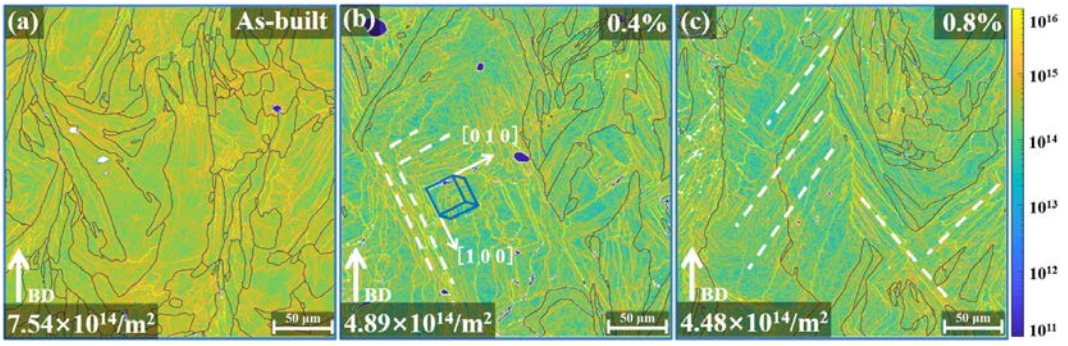

Fig. 15 Geometrically necessary dislocation distribution of (a) as-built, (b) 0.4% LCF, and (c) 0.8% LCF.

From Fig. 15(b) and (c), numerous orthogonal lines (near dotted lines) can be seen clearly in columnar grains, corresponding to the cell walls of the cellular sub-structure [61]. The walls become more distinct after cyclic loading, illustrating dislocations concentrating on the cell walls during dislocation movement. In addition, the GND concentration lines are almost at 45° to the build direction, also proving that cellular sub-structure grows along the 45° of build direction. In addition, Fig. 16(a) shows the distribution of misorientation angle among grains. The occurrence of HAGBs which includes critical grain boundary angle (15° usually) decreases after fatigue loading. As is shown in Fig. 16(b), grain size (equivalent diameter) also increases slightly after low cycle fatigue loading. The decreasing of HAGBs is closely related to grain coarsening. However, the so sight coarsening of grains (about 1μm difference) is less likely to cause cyclic softening. The occurrence of LAGBs in as-built 316L is about 3.13×105, decreasing to 1.23×105 and 1.12×105 after testing at 0.4% and 0.8% strain amplitudes, respectively. The large amount of LAGBs is a key factor causing high YS in SLM 316L. The annihilation of LAGBs during fatigue loading reduces the contribution to yield strength [59], leading to the observed cyclic softening.

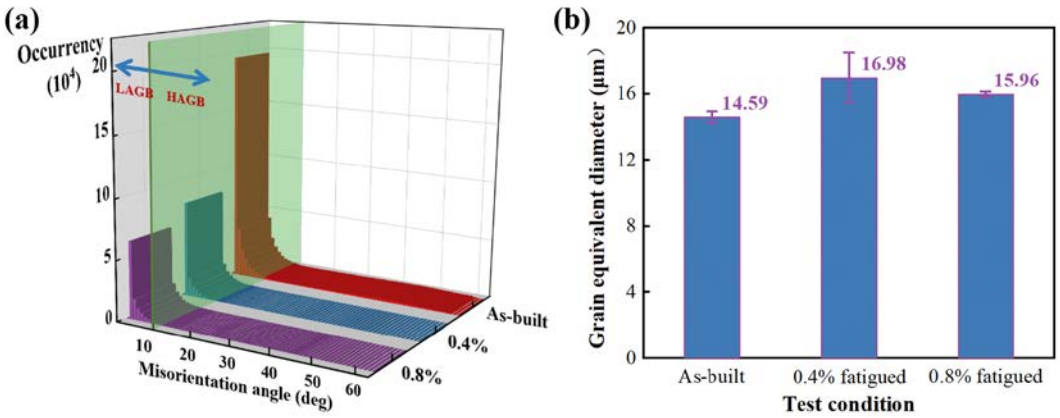

Fig. 16 (a) Misorientation angle distribution, and (b) grain diameter of as-built, 0.4 and 0.8% post-fatigue SLM 316L samples.

In summary, the cyclic softening behavior of SLM 316L can be contributed to these evolution of microstructure: (ⅰ) coarsening of the cellular sub-structure, (ⅱ) texture evolution from ＜111＞∥LD to ＜001＞∥LD, and (ⅲ) decrease of GND density and LAGBs during fatigue. More obvious evolution can be seen at higher strain amplitude, indicating more strength reduction after fatigue loading. However, the degree of softening (DOS) decreases with an increase in the strain amplitude. This phenomenon is contrary to the microstructural evolution in traditional cyclic softening materials[53, 55]. For traditional 316 type material, more obvious cyclic hardening behavior can be seen under higher strain amplitude due to interaction of dislocations, precipitates and solid solution atoms during plastic deformation [16, 62]. The degree of hardening (DOH) increases with increasing strain amplitude in traditional 316

type material [63]. As for SLM 316L, the larger plastic deformation at higher strain amplitude will promote cyclic hardening, leading to a reduction in the DOS with the strain amplitude. In Fig. 6(a), the initial cyclic hardening in first few cycles which appears only at high strain amplitudes (0.8 and 1.0%) also proves that. As for prior cold worked 316L which also have very high density of dislocations, the negative relationship between the DOS and strain amplitude can also been seen [64].

4.4 Fatigue cracking mechanism

In the SLM process, lack-of-fusion defect will occur when the powder cannot be completely melted caused by too fast scanning speed, or too large scanning distance[65]. Commonly, the lack-of-fusion defects have sharp edges and relatively lager volume. During the cyclic loading, the stress at the edge of a lack-of-fusion defect has a higher value than the remote stress[66]. This stress concentration causes fatigue cracks to nucleate preferentially at the location of lack-of-fusion defects. So, the fatigue cracks initiate from the lack-of-fusion near the surface at the strain amplitudes of 0.4, 0.6 and 0.8%. In addition, the cracks can also initiate from the oxide layer on the surface. The oxide layer is clearly observed in the blue line box, confirming the formation of an oxide layer at 550℃ (no oxide layer can be observed on the lack-of-fusion defects which are not exposed to the air shown in Fig. 9(i) (l)). The fracture of an oxide layer can also provide an initiation site for fatigue cracks in traditional 316L. It is believed that fracture of the oxide layer led to the crack initiation from the subsurface of the SLM 316L in the above case. These results show that near-surface lack-of-fusion defects are dangerous and should be avoided.

As is shown in Fig. 9(m-o), the spacing of coarse striation, increases with strain amplitude, indicating the expansion of the plastic region per cycle due to higher strain amplitude and continuously decreasing strength. Secondary cracks (orange circle in Fig. 9) can also be seen in the striations. Increased secondary cracking occurs at higher strain amplitude, because higher strain amplitude would create larger plastic deformation. In addition, the plastic deformation concentrates and leads to the initiation of secondary cracks near the edge of defects. The lack-of-fusion defects promotes the propagation of secondary cracks.

Interestingly, the fatigue striations are aligned to the build direction as shown by the purple arrows in Fig. 9. In contrast to the isotropic homogeneity of traditional 316L, the SLM 316L has mainly columnar grains parallel with the build direction. The effect of columnar grains on crack propagation is shown in Fig. 17(a). When a crack initiates on the top surface (parallel to build direction), the crack can propagate rapidly. However, when a crack initiates on a lateral surface, it will meet many grain boundaries which act as obstacles to propagation. As shown in Fig. 17(b), cracks need to climb over columnar grains when propagating along the perpendicular direction to BD. The fatigue crack propagation rate along the BD will thus be higher.

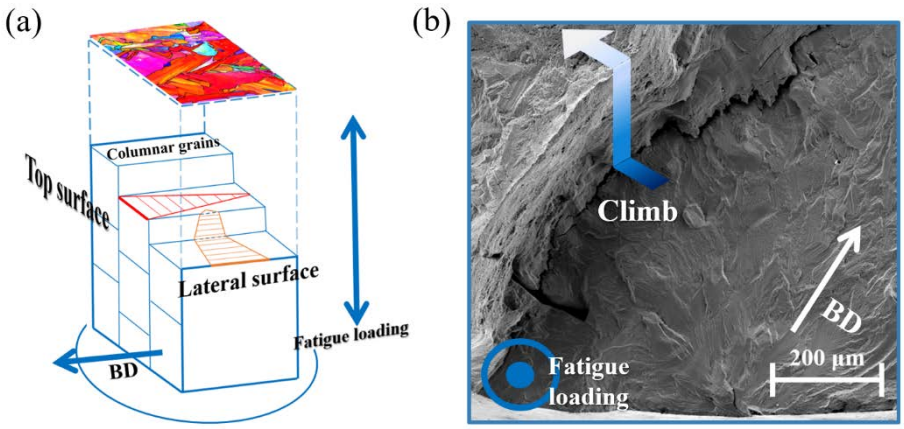

Fig.17 The schematic diagram of fatigue cracks propagating.

4.5 Life prediction

To predict LCF life accurately, a plastic strain energy model based on stable hysteresis loops was established by Lefebvre et al [57]. Each material has the capacity to dissipate a certain amount of energy, and when the limit is attained cracks propagate and failure occurs. The fatigue damage is generally associated with the accumulation of the plastic strain energy during fatigue cycling [67]. The plastic strain energy plays an important role in fatigue life prediction. During fatigue cycling, the hysteresis loop (whose area represents plastic strain energy per cycle) stabilizes after initial cyclic softening. Hence, the hysteresis loop at half-life can be used for calculating plastic strain energy and LCF life prediction. For Masing type materials, the plastic strain energy ΔW_p is defined as:

$$\Delta W_p = \left(\frac{1-n'}{1+n'}\right)\Delta\sigma\Delta\varepsilon_p \tag{5}$$

where $\Delta\sigma$ is stress amplitude, $\Delta\varepsilon_p$ is plastic strain amplitude, and n' is the cyclic strain hardening exponent.

For non-Masing type materials, as in this study, a Master curve can be achieved by overlapping the hysteresis loop tensile stages for different strain amplitudes, as shown in Fig.18(a). To describe the master curve, the following equation is used:

$$\frac{\Delta\varepsilon_p}{2} = \left(\frac{\Delta\sigma^*}{2K^*}\right)^{1/n^*} \tag{6}$$

where $\Delta\sigma^*$ and $\Delta\varepsilon_p$ is the stress amplitude and plastic strain amplitude respectively on the master curve. n^* is 0.195, this is different from *n'* of the Ramberg-Osgood relationship. The equation to calculate the plastic strain energy for non-Masing material is given by:

$$\Delta W_p = \left(\frac{1-n^*}{1+n^*}\right)\Delta\sigma\Delta\varepsilon_p + \left(\frac{2n^*}{1+n^*}\right)\delta\sigma_0\Delta\varepsilon_p \tag{7}$$

where $\delta\sigma_0$ is the proportional stress changes of lower tips under different strain amplitudes (shown in Fig. 18(a)). For Masing and non-Masing type materials, the relationship between life cycle and plastic strain energy under different strain amplitudes can be expressed as Coffin-Manson relationship[68]:

$$\Delta W_p N_f{}^{\beta} = C \tag{8}$$

where β and C are constants depending on material and achieved by experimental plastic strain energy ΔW_p and experimental fatigue life N_f. The values of β, C are 0.736, 374.28, respectively. After acquiring relationship between plastic strain energy and fatigue life from experiments, the predictive fatigue life can be obtained by inserting the calculated ΔW_p into the relationship. The calculated ΔW_p based on Masing and non-Masing behavior would lead to different predicted fatigue lives. As shown in Fig. 18(b), the predicted fatigue life for the non-Masing model is slightly more accurate than for the Masing model, proving that SLM 316L is non-Masing material. The non-Masing behavior in SLM 316L can be attributed to the microstructural instability during cyclic deformation.

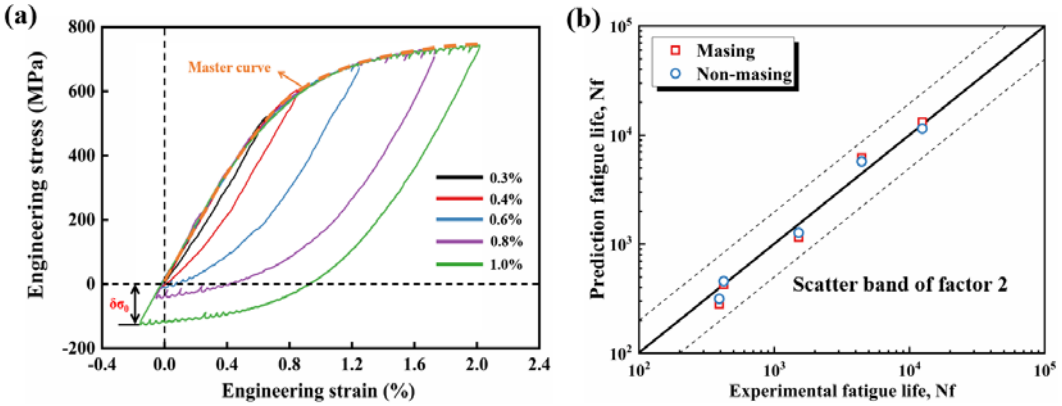

Fig. 18 (a) Construction of Master curve; (b) Fatigue life prediction using the plastic strain energy.

5. Conclusions

In this work, 316L LCF specimens have been manufactured by SLM technology, using commercial standard parameters that offered a minimum amount of porosity. LCF tests are conducted on the nearly full dense specimens at 550℃ high-temperature. Based on these tests, the LCF properties, microstructure evolution, crack behavior, fracture morphology, and life prediction are discussed in detail. Several conclusions on the LCF properties of SLM 316L can be drawn from this work:

1. SLM 316L has higher strength (YS 568 MPa and UTS 693 MPa) and lower ductility (elongation 52%) compared with traditional 316L. The yield strength of SLM 316L is 1.9 times of traditional 316L while the elongation meets the ASTM standard 35% for wrought 316L. The high strength is mainly attributed to the (i) cellular substructure, (ii) high dislocation density, and (iii) high content of LAGB, formed by the high cooling rate.
2. SLM 316L has better LCF properties than traditional 316L. It has longer life at 0.3, 0.4 and 0.6% strain

amplitudes and similar life at 0.8 and 1.0% strain amplitudes. It has significantly higher stress amplitude (cyclic strength) than traditional 316L and more stable cyclic (softening) behavior which is beneficial for engineering applications.

3. The cyclic softening behavior of SLM 316L is mainly attributed to: (ⅰ) coarsening of the cellular sub-structure, (ⅱ) texture evolution from ＜111＞ ∥ LD to ＜001＞ ∥ LD, and (ⅲ) decrease of GND density and LAGBs during fatigue. Because of the instability of the microstructure, SLM 316L has non-Masing behavior.
4. A transgranular fracture mode is observed across a range of strain amplitudes in SLM 316L. At higher strain amplitudes, fatigue cracks are fewer, shorter and wider. The melt boundaries have no obvious effect on resistance or promotion of crack propagation. Fatigue cracks originate from lack-of-fusion defects near the surface of all strain amplitudes. At lower strain amplitudes (0.4%), oxide layer can also act as crack initiation sites. The propagation direction for fatigue cracks is parallel to the build direction due to columnar grains in the microstructure.
5. Life prediction based on the non-Masing model is shown to be slightly more accurate than the Masing model, confirming that SLM 316L is a non-Masing material.

Acknowledgment

The authors gratefully acknowledge the financial support of the Key Project of University Natural Science Research in Jiangsu province (20KJA460002), Postgraduate Research & Practice Innovation Program of Jiangsu Province (KYCX21_1119). X. Yang and S. Leen also acknowledge the financial support of Science Foundation Ireland as part of I-Form Advanced Manufacturing Research Centre under grant number SFI/16/RC/3872.

References:

[1]. Herzog, D., et al., Additive manufacturing of metals. Acta Materialia, 2016. 117: p. 371-392.

[2]. Bartlett, J.L. and X. Li, An overview of residual stresses in metal powder bed fusion. Additive Manufacturing, 2019. 27: p. 131-149.

[3].Fereiduni, E., A. Ghasemi and M. Elbestawi, Selective Laser Melting of Aluminum and Titanium Matrix Composites: Recent Progress and Potential Applications in the Aerospace Industry. Aerospace, 2020. 7(6): p. 77.

[4]. Vaithilingam, J., et al., Surface chemistry of Ti6Al4V components fabricated using selective laser melting for biomedical applications. Materials Science and Engineering: C, 2016. 67: p. 294-303.

[5]. Fu, C., et al., Effect of helium bubbles on irradiation hardening of additive manufacturing 316L stainless steel under high temperature He ions irradiation. Journal of Nuclear Materials, 2021. 550: p. 152948.
[6]. Fu, J., et al., Comparison of the microstructure, mechanical properties and distortion of stainless steel 316 L fabricated by micro and conventional laser powder bed fusion. Additive Manufacturing, 2021. 44: p. 102067.
[7]. Lewandowski, J.J. and M. Seifi, Metal Additive Manufacturing: A Review of Mechanical Properties. Annual review of materials research, 2016. 46(1): p. 151-186.
[8]. Hong, S., The tensile and low-cycle fatigue behavior of cold worked 316L stainless steel: influence of dynamic strain aging. International Journal of Fatigue, 2004. 26(8): p. 899-910.
[9]. Dahlberg, M. and D. Bremberg, Fatigue margins for austenitic stainless steels in ASME Boiler and pressure vessel code–a literature study. Stral Sakerhets Myndigheten Swedish Radiation Safety Authority, 2012.
[10]. Zhong, Y., et al., Intragranular cellular segregation network structure strengthening 316L stainless steel prepared by selective laser melting. Journal of Nuclear Materials, 2016. 470: p. 170-178.
[11]. Chen, W., P. Spätig and H.P. Seifert, Role of mean stress on fatigue behavior of a 316L austenitic stainless steel in LWR and air environments. International Journal of Fatigue, 2021. 145: p. 106111.
[12]. Gerland, M., et al., Low cycle fatigue behaviour in vacuum of a 316L-type austenitic stainless steel between 20 and 600°C—Part II: Dislocation structure evolution and correlation with cyclic behaviour. Materials science & engineering. A, Structural materials : properties, microstructure and processing, 1997. 229(1): p. 68-86.
[13]. Mohammad, K.A., et al., Fatigue behavior of Austenitic Type 316L Stainless Steel. IOP conference series. Materials Science and Engineering, 2012. 36: p. 12012.
[14]. Yan, X., et al., Review of creep–fatigue endurance and life prediction of 316 stainless steels. International Journal of Pressure Vessels and Piping, 2015. 126-127: p. 17-28.
[15]. Srinivasan, V.S., et al., Effect of hold-time on low cycle fatigue behaviour of nitrogen bearing 316L stainless steel. The International journal of pressure vessels and piping, 1999. 76(12): p. 863-870.
[16]. Srinivasan, V.S., Low cycle fatigue and creep–fatigue interaction behavior of 316L(N) stainless steel and life prediction by artificial neural network approach. International Journal of Fatigue, 2003. 25(12): p. 1327-1338.
[17]. Srinivasan, V.S., et al., The influence of dynamic strain ageing on stress response and strain-life relationship in low cycle fatigue of 316L(N) stainless steel. Scripta materialia, 1997. 37(10): p. 1593-1598.
[18]. Sasikala, G., et al., Creep deformation and fracture behavior of types 316 and 316L(N) stainless steels and their weld metals. Metallurgical and materials transactions. A, Physical metallurgy and materials science, 2000. 31(4): p. 1175-1185.
[19]. Srinivasan, V.S., et al., High temperature time-dependent low cycle fatigue behaviour of a type 316L(N) stainless steel. International journal of fatigue, 1999. 21(1): p. 11-21.
[20]. Srinivasan, V.S., Comparative evaluation of strain controlled low cycle fatigue behaviour of solution annealed and prior cold worked 316L(N) stainless steel. International Journal of Fatigue, 2004. 26(12): p. 1295-1302.
[21]. Kruth, J., et al., New ferro powder for selective laser sintering of dense parts. CIRP Annals, 2003, 52(1): p.139-142.
[22]. Wang, Y.M., et al., Additively manufactured hierarchical stainless steels with high strength and ductility. Nature Materials, 2018. 17(1): p. 63-71.
[23]. Pham, M., et al., The role of side-branching in microstructure development in laser powder-bed fusion. Nature Communications, 2020. 11(1).
[24]. Shamsujjoha, M., et al., High Strength and Ductility of Additively Manufactured 316L Stainless Steel Explained. Metallurgical and materials transactions. A, Physical metallurgy and materials science, 2018. 49(7): p. 3011-3027.
[25]. Voisin, T., et al., New insights on cellular structures strengthening mechanisms and thermal stability of an austenitic stainless steel fabricated by laser powder-bed-fusion. Acta Materialia, 2021. 203: p. 116476.
[26]. Yan, F., et al., Characterization of nano-scale oxides in austenitic stainless steel processed by powder bed fusion. Scripta Materialia, 2018. 155: p. 104-108.
[27]. Wood, P., et al., Influences of Horizontal and Vertical Build Orientations and Post-Fabrication Processes on the

Fatigue Behavior of Stainless Steel 316L Produced by Selective Laser Melting. Materials, 2019. 12(24): p. 4203.
[28]. Stern, F., et al., Investigation of the anisotropic cyclic damage behavior of selective laser melted AISI 316L stainless steel. Fatigue & Fracture of Engineering Materials & Structures, 2019. 42(11): p. 2422-2430.
[29]. Afkhami, S., et al., Fatigue characteristics of steels manufactured by selective laser melting. International Journal of Fatigue, 2019. 122: p. 72-83.
[30]. Elangeswaran, C., et al., Microstructural analysis and fatigue crack initiation modelling of additively manufactured 316L after different heat treatments. Materials & Design, 2020. 194: p. 108962.
[31]. Hatami, S., et al., Fatigue Strength of 316 L Stainless Steel Manufactured by Selective Laser Melting. Journal of Materials Engineering and Performance, 2020. 29(5): p. 3183-3194.
[32]. Elangeswaran, C., et al., Effect of post-treatments on the fatigue behaviour of 316L stainless steel manufactured by laser powder bed fusion. International Journal of Fatigue, 2019. 123: p. 31-39.
[33]. Han, W., et al., Orientation effect of electropolishing characteristics of 316L stainless steel fabricated by laser powder bed fusion. Frontiers of Mechanical Engineering, 2021. 16(3): p. 580-592.
[34]. Benedetti, M., et al., The effect of post-sintering treatments on the fatigue and biological behavior of Ti-6Al-4V ELI parts made by selective laser melting. Journal of the Mechanical Behavior of Biomedical Materials, 2017. 71: p. 295-306.
[35]. Andreau, O., et al., Influence of the position and size of various deterministic defects on the high cycle fatigue resistance of a 316L steel manufactured by laser powder bed fusion. International Journal of Fatigue, 2021. 143: p. 105930.
[36]. Zhang, M., et al., Predictive models for fatigue property of laser powder bed fusion stainless steel 316L. Materials & Design, 2018. 145: p. 42-54.
[37]. Damiens, A., H. Bonnefoy and I. Titeux, Influence of processing parameters on mechanical and fatigue properties of 316L steel manufactured by selective laser melting. Welding in the World, 2020. 64(8): p. 1321-1328.
[38]. Blinn, B., et al., Determination of the influence of a stress-relief heat treatment and additively manufactured surface on the fatigue behavior of selectively laser melted AISI 316L by using efficient short-time procedures. International Journal of Fatigue, 2020. 131: p. 105301.
[39]. Zhang, H., et al., Role of local recrystallization behavior on fatigue performance of SLMed 304L austenitic stainless steels. Materials Characterization, 2021. 177: p. 111159.
[40]. Pegues, J.W., M.D. Roach and N. Shamsaei, Additive manufacturing of fatigue resistant austenitic stainless steels by understanding process-structure-property relationships. Materials research letters, 2020. 8(1): p. 8-15.
[41]. ASTM International, F3184-16 Standard Specification for Additive Manufacturing Stainless Steel Alloy (UNS S31603) with Powder Bed Fusion, ASTM International, West Conshohocken, PA, 2016.
[42]. Zhu, C., et al., Dislocation-type evolution in quasi-statically compressed polycrystalline nickel. Acta Materialia, 2018. 155: p. 104-116.
[43]. Muránsky, O., et al., On the measurement of dislocations and dislocation substructures using EBSD and HRSD techniques. Acta Materialia, 2019. 175: p. 297-313.
[44]. Pantleon, W., Resolving the geometrically necessary dislocation content by conventional electron backscattering diffraction. Scripta Materialia, 2008. 58(11): p. 994-997.
[45]. Cui, L., et al., Revealing relationships between microstructure and hardening nature of additively manufactured 316L stainless steel. Materials & Design, 2021. 198: p. 109385.
[46]. Totemeier, T.C. and H. Tian, Creep-fatigue–environment interactions in INCONEL 617. Materials Science and Engineering: A, 2007. 468-470: p. 81-87.
[47]. Zhang, T., et al., P92 steel creep-fatigue interaction responses under hybrid stress-strain controlled loading and a life prediction model. International Journal of Fatigue, 2020. 140: p. 105837.
[48]. Kim, D.W., J. Chang and W. Ryu, Evaluation of the creep–fatigue damage mechanism of Type 316L and Type 316LN stainless steel. International Journal of Pressure Vessels and Piping, 2008. 85(6): p. 378-384.
[49]. Wang, X., et al., Characterization of Low Cycle Fatigue Performance of New Ferritic P92 Steel at High Temperature:

Effect of Strain Amplitude. steel research international, 2015. 86(9): p. 1046-1055.
[50]. Segura, I.A., et al., Grain boundary and microstructure engineering of Inconel 690 cladding on stainless-steel 316L using electron-beam powder bed fusion additive manufacturing. Journal of Materials Science & Technology, 2019. 35(2): p. 351-367.
[51]. Kong, D., et al., Bio-functional and anti-corrosive 3D printing 316L stainless steel fabricated by selective laser melting. Materials & Design, 2018. 152: p. 88-101.
[52]. ASTM International, ASTM A312-17 Standard Specification for Seamless, Welded, and Heavily Cold Worked Austenitic Stainless Steel Pipes, ASTM International, West Conshohocken, PA, 2017.
[53]. Jing, H., et al., Low cycle fatigue behavior and microstructure evolution of a novel 9Cr–3W–3Co tempered martensitic steel at 650 °C. Materials Science and Engineering: A, 2018. 731: p. 394-402.
[54]. Tang, H., et al., Multi-Scale modelling of structure-property relationship in additively manufactured metallic materials. International Journal of Mechanical Sciences, 2021. 194: p. 106185.
[55]. ZHANG, Z., et al., Low Cycle Fatigue Behavior and Cyclic Softening of P92 Ferritic-martensitic Steel. Journal of iron and steel research, international, 2015. 22(6): p. 534-542.
[56]. Goyal, S., et al., A comparative assessment of fatigue deformation behavior of 316 LN SS at ambient and high temperature. Materials Science and Engineering: A, 2017. 696: p. 407-415.
[57]. Lefebvre, D., et al., Cyclic response and inelastic strain energy in low cycle fatigue. International Journal of Fatigue. 1984. 6(1): p. 9-15.
[58]. Yin, H., et al., Thermal stability and microstructural evolution of additively manufactured 316L stainless steel by laser powder bed fusion at 500–800 ℃. Additive Manufacturing, 2021. 41: p. 101981.
[59]. Wang, X., et al., Crystallographic-orientation-dependent tensile behaviours of stainless steel 316L fabricated by laser powder bed fusion. Materials Science and Engineering: A, 2019. 766: p. 138395.
[60]. Suwas, Satyam, and Ranjit Kumar Ray. Crystallographic texture of materials. London: Springer, 2014.
[61]. Krakhmalev, P., et al., Microstructure, Solidification Texture, and Thermal Stability of 316 L Stainless Steel Manufactured by Laser Powder Bed Fusion. Metals, 2018. 8(8): p. 643.
[62]. Shankar, V., et al., Understanding low cycle fatigue and creep–fatigue interaction behavior of 316 L(N) stainless steel weld joint. International Journal of Fatigue, 2016. 82: p. 487-496.
[63]. Roy, S.C., et al., Low cycle fatigue life prediction of 316 L(N) stainless steel based on cyclic elasto-plastic response. Nuclear Engineering and Design, 2012. 253: p. 219-225.
[64]. Hong, Seong-Gu, et al., The effect of temperature on low-cycle fatigue behavior of prior cold worked 316L stainless steel. International Journal of Fatigue 2003. 25.9-11: p. 1293-1300.
[65]. Li, W.B., et al., The high-cycle fatigue properties of selective laser melted Inconel 718 at room and elevated temperatures. Materials Science and Engineering: A, 2022. 836: p. 142716.
[66]. Murakami, Y., Chapter 2 - Stress Concentration, in Metal Fatigue, Y. Murakami, Y. Murakami^Editors. 2002, Elsevier Science Ltd: Oxford. p. 11-24.
[67]. Zhang, J., et al., Low cycle fatigue of 2.25Cr1Mo steel with tensile and compressed hold loading at elevated temperature. Materials Science and Engineering: A, 2016. 667: p. 251-260.
[68]. Jing, H., et al., Low cycle fatigue behavior and microstructure evolution of a novel 9Cr–3W–3Co tempered martensitic steel at 650 °C. Materials Science and Engineering: A, 2018. 731: p. 394-402.